

Density-Dependent Transition in Bacterial Self-Organization Driven by Confinement and Aerotaxis

Minjun Kim¹ and Joonwoo Jeong^{1,2,*}

¹*Department of Physics, Ulsan National Institute of Science and Technology, Ulsan, Republic of Korea*

²*UNIST Center for Soft and Living Matter, Ulsan, Korea*

(Dated: March 17, 2026)

We experimentally investigate how aerotactic bacteria, confined within a thin liquid film between two solid substrates, respond to a controlled oxygen gradient. We find that the total bacterial number density dictates which mechanism dominates the steady-state spatial distribution: wall accumulation or aerotaxis. At low densities, despite receiving oxygen only from one substrate, motile bacteria accumulate at both walls, forming a symmetric distribution. In contrast, pronounced aerotactic migration toward the oxygen-supplying wall emerges as the density increases. Analyzing the temporal evolution of this bacterial distribution reveals that the aerotactic response is driven by a self-generated oxygen gradient induced by collective respiration. Our diffusion-advection model of bacteria and oxygen, accounting for aerotactic migration, hydrodynamic attraction to the walls, and respiration, quantitatively reproduces our experimental observations and provides valuable insights into bacterial self-organization within complex environments.

I. INTRODUCTION

Microorganisms often navigate heterogeneous environments where survival depends on their ability to adapt [1–5]. Key strategies involve sensing local environments and migrating toward favorable conditions. For instance, in response to oxygen gradients, aerobic bacteria may perform aerotaxis by biasing their random-walk motility; they can adjust their tumble rate when moving up an attractant gradient [1, 6–9]. In addition to chemical signals, microorganisms frequently encounter physical boundaries in both natural and engineered settings. Near these surfaces, a combination of hydrodynamic interactions and persistent self-propulsion leads to significant cell accumulation [10–13]. This wall-trapping effect extends residence times at the surface, which in turn increases the probability of surface adhesion and facilitates the critical early stages of bacterial biofilm formation [14–16].

Bacteria actively reorganize their populations spatiotemporally, responding to and even shaping their complex surroundings. These self-organization phenomena have been studied by varying external stimuli [17–21] and confining geometries [10, 22–26], or by designing rectifying structures [27–31]—approaches that have attracted increasing attention for controlling microbial dynamics. Microfluidic devices [9, 32–34] and capillary tubes [7, 35–37] have been employed as experimental platforms to study such self-organization, exemplified by traveling bacterial bands, which often emerge from an interplay between the bacterial consumption of limited resources, such as oxygen or nutrients, and the local depletion caused by an insufficient and asymmetric supply. In a similar vein, microbial dynamics in nature-mimicking environments featuring strong confinement have garnered

significant interest [5, 38–40].

In this work, we introduce a strongly confined one-dimensional system subject to a controlled oxygen supply to investigate the spatiotemporal distribution of aerotactic bacteria. Combining systematic experiments that vary the oxygen gradient and bacterial number density with a diffusion-advection model accounting for bacteria-wall interactions and aerotaxis, we reveal an underlying mechanism behind the density-dependent transition in bacterial self-organization: the competition between wall accumulation and a self-generated oxygen gradient. These findings demonstrate how bacterial populations actively modify their chemical environment, leading to emergent collective behaviors that depend critically on population density within confined, resource-limited systems.

II. RESULTS AND DISCUSSION

We investigate the spatial distribution of motile bacteria in a thin liquid film as a function of total bacterial density. Aerotactic bacteria, *Bacillus subtilis*, are confined in a cylindrical well with an 80–100 μm height and 8 mm diameter. As shown in Fig. 1(a), the top boundary is covered with an oxygen-permeable coverslip, while all the other boundaries of the cylindrical well are oxygen-impermeable; the oxygen is supplied exclusively to the top interface. We divide the film into 11 vertical sections, including the top and bottom boundaries, count the number of swimming bacteria in each section, and measure the one-dimensional distribution function of swimming bacteria; see Materials and Methods for details.

At low number densities such as 3.5×10^7 cells/mL (Fig. 1(b), blue squares), we observe a symmetric bacterial distribution along the vertical axis, with population peaks at both top and bottom boundaries: wall accumulation. The symmetric profile in confinement is primarily attributed to the interaction between motile bacteria

* jjeong@unist.ac.kr

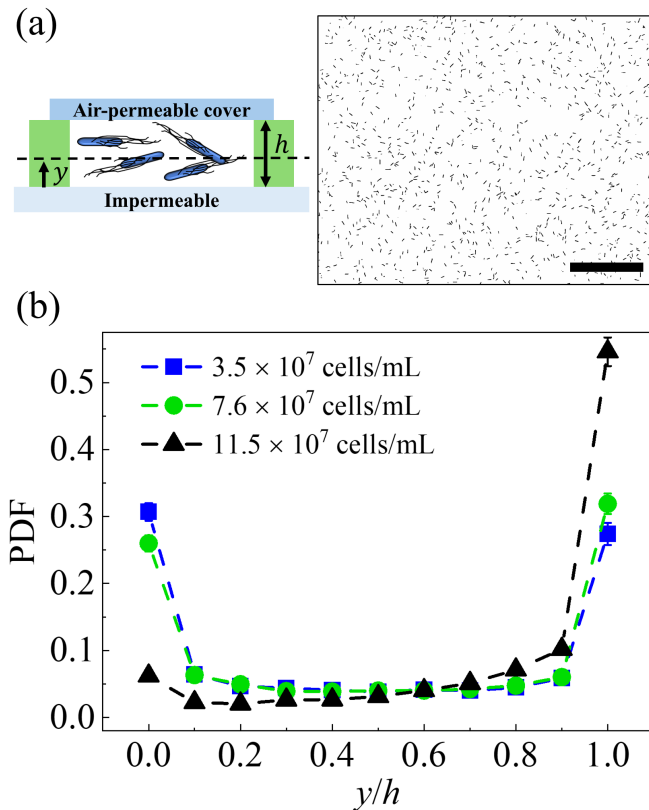


FIG. 1. Experimental setup and steady-state bacterial distributions for different number densities. (a) Left: A schematic illustrating the confinement geometry. Bacteria are confined in a thin liquid film of height h between a top oxygen-permeable coverslip and a bottom impermeable substrate. Right: A representative binary image of bacteria at high density near the oxygen-permeable top boundary. The scale bar is $100 \mu\text{m}$. (b) Probability distribution functions (PDFs) of bacterial counts at steady state for three different number densities. The PDFs are plotted against the normalized vertical position, y/h . The error bars represent the standard deviation of the temporal fluctuations in the bacterial count at each position, calculated over the recording period.

and solid boundaries, driven by two key mechanisms: directional persistence and hydrodynamic interactions with boundaries [10, 11]. The former describes the tendency of bacteria to maintain their swimming direction upon encountering an interface, whereas the latter arises from the flow field generated by the rotating flagella modeled as the hydrodynamic dipoles. Pusher-type swimmers, such as the observed *B. subtilis*, exhibit an effective attraction toward the boundary; consequently, the wall accumulation [10, 41].

As the bacterial number density increases, the spatial distributions in Fig. 1(b) change from symmetric to asymmetric, featuring a pronounced peak near the top oxygen-supplied boundary and a sparse population at the bottom. Given that oxygen is supplied exclusively from the top interface, this asymmetry is attributed to aerotaxis strong enough to overcome the wall accumula-

tion effect. A series of control experiments, including one with a gas-controlled chamber (Sup. Fig. 1 and 2), confirms that aerotaxis is the primary driver of the observed asymmetric organization. Based on these findings, the total bacterial number density B_{tot} is the key parameter that determines the balance between wall accumulation and aerotaxis in this confined, resource-limited environment. Notably, a supplementary experiment with induced spatial inhomogeneity (Sup. Fig. 3) demonstrates that the steady-state distribution is set by the total population and global oxygen balance rather than local density variations.

Temporal evolution measurements in high-density suspensions (11.7×10^7 cells/mL) suggest a self-generated oxygen gradient as the mechanism underlying the total density-dependent spatial distribution. As shown in Fig. 2(a), an initially symmetric, wall-accumulation-dominated distribution transitions to an asymmetric steady state governed by aerotactic migration as time goes by. In contrast, low-density suspensions maintain their symmetric distribution throughout the observation period (Sup. Fig. 4), indicating that significant collective respiration is required to generate oxygen depletion and vertical gradients, thus breaking the spatial symmetry. This observation is consistent with previous studies showing that motile bacteria in confinement create self-organized patterns by consuming local resources [7, 37, 42].

Synthesizing these findings, we propose a conceptual model to explain the observation (Fig. 2(b)). The symmetric, wall-dominated distribution develops when the oxygen concentration is uniform. As respiration proceeds, oxygen is preferentially depleted near the oxygen-impermeable interface, establishing an oxygen-concentration gradient. In high-density suspensions, where the collective consumption rate exceeds the oxygen-supply flux from the oxygen-permeable interface, this self-generated gradient drives a migration toward the oxygen-rich region via aerotaxis, resulting in an asymmetric steady-state profile. At low density, however, the respiration rate remains below the replenishment rate, and the bacterial population does not experience a strong enough oxygen gradient, so it maintains a symmetric distribution. Ultimately, the total bacterial number density determines whether the system is governed by wall accumulation or by emergent, self-generated oxygen gradients.

To rationalize our experimental results, we develop a continuum model based on the Keller-Segel framework, which describes the coupled dynamics of motile bacteria and a chemoattractant (oxygen) [43, 44]. The following advection-diffusion equation describes the spatiotemporal evolution of the one-dimensional bacterial density, $B(y, t)$ along the spatial axis (y):

$$\frac{\partial B(y, t)}{\partial t} = \frac{\partial}{\partial y} \left[D_{\text{bac}} \frac{\partial B(y, t)}{\partial y} - u(y, t) B(y, t) \right] \quad (1)$$

where D_{bac} is the bacterial diffusion coefficient represent-

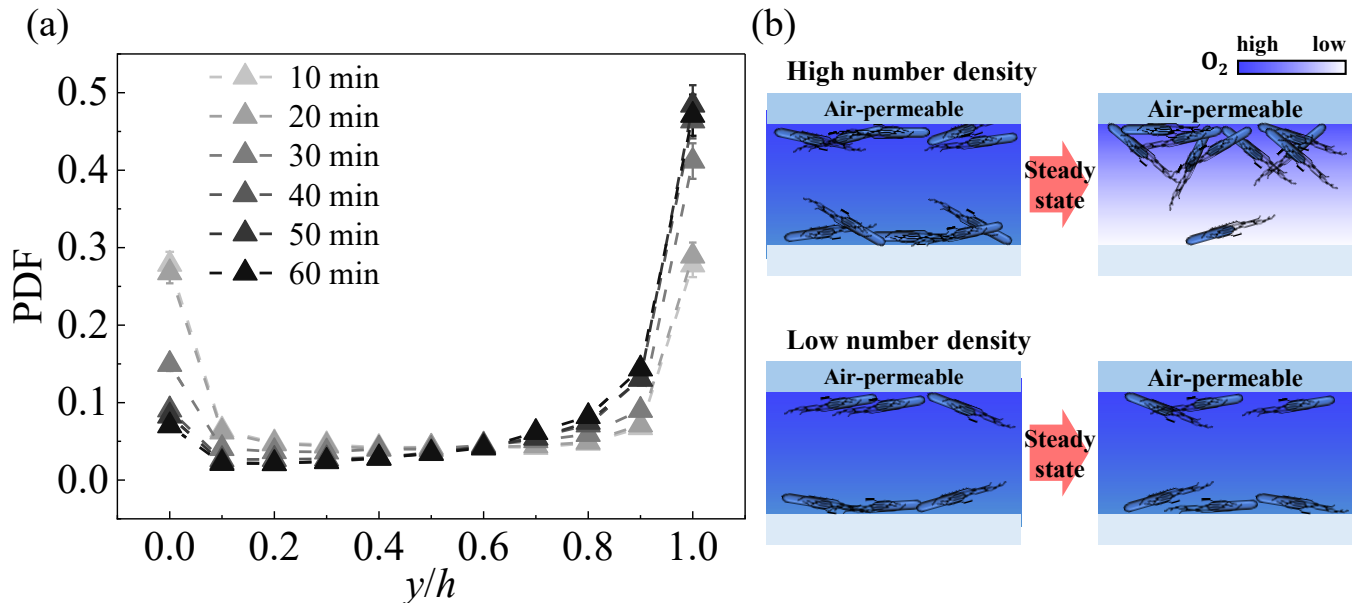


FIG. 2. Temporal evolution of the bacterial distribution at high density and a schematic of the system dynamics. (a) PDFs of bacterial counts for a high-density suspension (11.7×10^7 cells/mL) measured at different time points, from 10 min (light gray triangles) to 60 min (black triangles). The error bars represent the standard deviation of temporal fluctuations in the bacterial count at each position, calculated over the recording period. (b) Schematic diagrams contrasting the system's evolution at high and low number densities. The top row depicts the high-density case, showing a transition from an initial symmetric distribution to an asymmetric steady state. The bottom row depicts the low-density case, showing the persistence of a symmetric distribution from the initial to the steady state. The color fill in the diagrams represents the oxygen concentration, which is defined by the legend in the top-right corner (labeled O_2); blue and white indicate high and low concentrations, respectively.

ing random motility of bacteria, and $u(y, t)$ is the directional migration velocity. The migration velocity in our model comprises two components: hydrodynamic velocity (u_{hydro}) and aerotactic velocity (u_{taxis}):

$$u(y, t) = u_{\text{hydro}} + u_{\text{taxis}}. \quad (2)$$

The hydrodynamic term describes the attraction of pusher-type swimmers to nearby surfaces, resulting in the wall accumulation, and the aerotactic term represents the biased migration up the oxygen concentration gradient:

$$u_{\text{hydro}} = -\frac{3p}{64\pi\eta} \left(\frac{1}{y^2} - \frac{1}{(h-y)^2} \right) \quad (3)$$

$$u_{\text{taxis}} = \chi \frac{\partial c(y, t) / \partial y}{(c(y, t) + K_{d1})(c(y, t) + K_{d2})} \quad (4)$$

where h is the sample height, p is the dipole strength of bacteria, η is viscosity, χ is aerotactic sensitivity, K_{d1} , K_{d2} are oxygen dissociation constants of *B. subtilis*, and $c(y, t)$ is local oxygen concentration [9, 10, 45]. To avoid the divergence of u_{hydro} at the boundaries ($y = 0$ and $y = h$), we adopt a regularized Stokeslet formulation, replacing $\frac{1}{y^2}$ and $\frac{1}{(h-y)^2}$ with $\frac{1}{y^2 + \epsilon^2}$ and $\frac{1}{(h-y)^2 + \epsilon^2}$, where ϵ is the blob size [46–48] (details in Supplementary Materials).

The oxygen concentration $c(y, t)$, which is governed by the oxygen diffusion and its consumption by bacteria, is

coupled to the bacterial density $B(y, t)$ via u_{taxis} . $c(y, t)$ follows

$$\frac{\partial c(y, t)}{\partial t} = D_{\text{oxy}} \frac{\partial^2 c(y, t)}{\partial y^2} - R(y, t)B(y, t), \quad (5)$$

where D_{oxy} is the diffusion coefficient of oxygen dissolved in water and $R(y, t) = \frac{R_0}{2} \left(\frac{c(y, t)}{c(y, t) + K_{d1}} + \frac{c(y, t)}{c(y, t) + K_{d2}} \right)$ is the oxygen respiration rate per bacterium, which depends on the local oxygen concentration [45].

We numerically solve two coupled, nondimensionalized partial differential equations for the steady state subject to appropriate boundary conditions and, as shown in Fig. 3, reproduce the density-dependent spatial distributions observed in the experiments. See Materials and Methods for the calculation details. We fit the experimental data numerically by minimizing the mean squared error (MSE) across the three densities and find all fitted parameters are within the range of previously reported values [9, 45, 49, 50]: $\chi = 2.0 \times 10^3$ M $\mu\text{m}^2/\text{s}$, $K_{d1} = 1.0$ μM , $K_{d2} = 100$ μM , $k = \frac{3p}{64\pi\eta} = 6.0 \times 10^2$ $\mu\text{m}^3/\text{s}$, $R_0 = 2.0 \times 10^6$ molecules/s per bacterium, and $\epsilon = 2$ μm . Here, the blob size includes the radius of the cell body and the flagella bundle. Fluorescence images of the flagellar bundle show a maximum width of ~ 7 μm , thus $\epsilon = 2$ μm lies within this range [51]. Note also that we adopt the diffusion coefficients for bacteria and oxygen

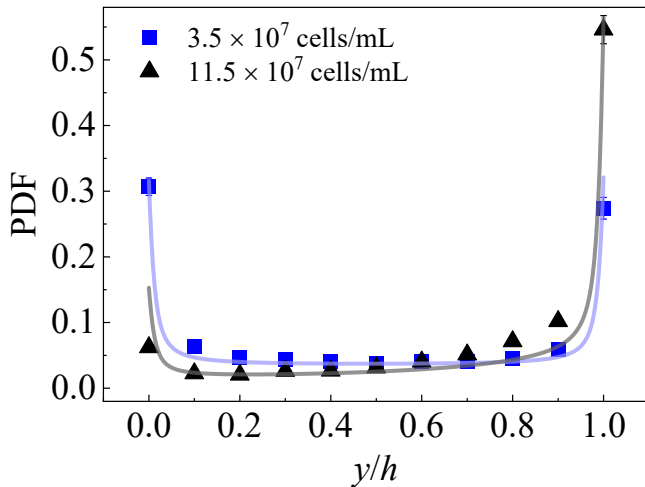


FIG. 3. Comparison between experimental bacterial distributions (symbols) and model predictions (solid lines) for low and high number densities. Two representative bacterial number densities in Fig. 1 are chosen for numerical fitting.

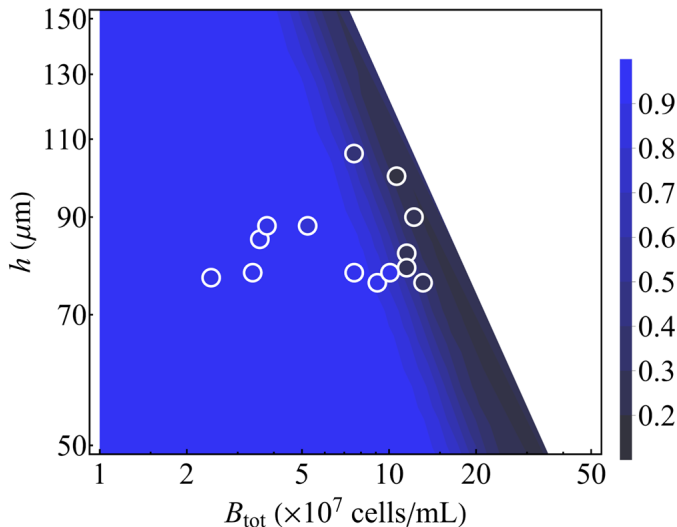


FIG. 4. The state diagram of bacterial distribution symmetry as a function of total bacterial number density (B_{tot}) and film height (h). The color scale shows the symmetry parameter (sym); darker colors indicate more asymmetric (aerotaxis-dominated) profiles. Regions of $sym < 0.17$ are omitted because the numerical solutions fail to satisfy the boundary conditions in this highly asymmetric regime. Experimental data are overlaid as circles which are color-coded with the experimentally estimated sym .

from reference [9], $D_{bac} = 2.1 \times 10^2 \mu\text{m}^2/\text{s}$, $D_{oxy} = 2 \times 10^3 \mu\text{m}^2/\text{s}$.

Beyond fitting the experimental data, we use our model to explore the parameter space defined by two primary control parameters, the total bacterial number density (B_{tot}) and film height (h). First, to quantify how symmetric the bacterial distribution is, we define a symmetry

parameter

$$sym = \min(L_S, U_S) / \max(L_S, U_S)$$

where $L_S = \int_0^{h/2} B(y) dy$ and $U_S = \int_{h/2}^h B(y) dy$. Thus, $sym = 1$ indicates perfect symmetry, whereas smaller values indicate stronger asymmetry. As shown in Fig. 4, we then calculate this symmetry parameter over a range of B_{tot} and h to generate a state diagram overlaid with experimental data. As explained, as the cell density B_{tot} increases, sym decreases because of the self-generated oxygen gradient. The dependence on film height (h) can be understood through the oxygen diffusion time, $\tau_{oxy} = h^2/D_{oxy}$. As the film gets thinner, the diffusion time gets shorter, meaning oxygen supplied from the top boundary can diffuse faster throughout the entire film. This rapid replenishment prevents the formation of strong depletion, thus weakening the aerotactic response and favoring a symmetric distribution. Our model calculation can be extended to a broader range of B_{tot} and h , including the bioconvection regime and extreme confinement effects, as detailed in the Supplementary Materials.

III. CONCLUSION

In conclusion, we have investigated bacterial self-organization under confinement subject to an inhomogeneous oxygen supply. The total bacterial number density dictates the dominant mechanism governing their spatial distribution: wall accumulation prevails at low densities, whereas a self-generated oxygen gradient, driven by collective bacterial respiration, induces aerotactic migration at high densities, leading to an asymmetric distribution. Our continuum model, combining the Keller–Segel framework with the hydrodynamic attraction of bacteria to surfaces, quantitatively reproduces this density-dependent transition across a broad range of bacterial densities and film heights.

Our work establishes a framework for understanding how bacterial populations respond to complex environments where chemical stimuli and physical confinement coexist. Given that such conditions — where bacteria simultaneously experience spatial restriction and resource limitation — are prevalent in their natural habitats, ranging from soil matrices to mucus layers, a predictive model of their combined effects is crucial for advancing our understanding of bacterial organization. Specifically, our findings offer insights into how confined bacteria not only respond to but also collectively shape their chemical environment, with potential implications for biofilm formation and survival strategies under inhospitable conditions. Furthermore, the density-dependent transition we observe may reflect a more general principle applicable across diverse spatiotemporal scales, such as animal populations competing for limited resources in spatially restricted habitats.

IV. MATERIALS AND METHODS

A. Bacterial cell culture

A single colony of *Bacillus subtilis* strain ATCC 6051 (wild type) was initially inoculated onto Lysogeny Broth (LB) agar and incubated overnight at 37 °C. The resulting culture was then transferred to Terrific Broth (TB) and grown overnight in a shaking incubator at 37 °C and 250 RPM. This diluted culture — with fresh TB to an optical density at 600 nm (OD600) of approximately 0.03 — was then incubated under the same conditions (37 °C, 250 RPM) until it reached the mid-exponential phase. To maximize cell yield, the culture was transferred to 15 mL tubes and centrifuged at 4000 RPM for 15 min, then resuspended in a final volume of 2 mL TB. To predominantly single, motile bacteria with minimal aggregated bacteria, the 1 mL solution was centrifuged at 6000 RPM for 1 min, and 800 μ L of the supernatant was carefully collected. Finally, this bacterial suspension was washed and resuspended in M9 minimal medium to reduce cell division during the observation.

B. Sample preparation

To construct the observation chamber, we sandwiched two substrates using aluminum double-sided tape (No. 791, Teraoka, Japan) as a spacer, which had an 8 mm diameter made by a biopsy punch (Miltex, Ted Pella, U.S.A.). We confirmed that the spacer and a glass substrate functioned as an oxygen barrier, while the other substrate, the coverslip (Cat. no. 10813, Ibidi, Germany), is oxygen-permeable. The drop-and-cover assembly with approximately 8.0 μ L of the bacterial suspension resulted in a confined liquid film with an approximate height of 80–100 μ m. Alternatively, in the number fluctuation experiment, the chamber was filled with bacterial suspension via capillary flow, i.e., instead of the drop-and-cover method, and sealed with epoxy (Loctite, Henkel, Germany). To generate a radial oxygen supply, we also used a PDMS-based sheet (SecureSeal, Grace Bio-Labs, U.S.A.) of 120 μ m thickness as an oxygen-permeable spacer. Experiments controlling the external oxygen concentration were conducted in a live-cell imaging chamber equipped with a gas-mixing chamber (Live Cell Instrument, Republic of Korea), which provided the chamber with a mixed gas of ambient air and nitrogen at a controlled ratio.

C. Optical microscopy and measurement

We observed bacteria using an inverted microscope (IX73, Olympus) equipped with 20X and 40X objective lenses and a CCD camera (INFINITY5, Teledyne Lumenera, Canada) in both bright-field and phase-contrast modes. To determine the bacterial distribution along the sample height, we counted bacteria at 11 distinct, equally spaced positions. This imaging range extended from the bottom impermeable boundary to the oxygen-permeable top cover of the sample. At each of these 11 positions, we recorded a 7-to-15-second-long movie at 30-50 frames per second.

To segment focused bacteria at each focal plane, we adopted Statistical Regional Merging (SRM) [52] and applied an appropriate threshold to the SRM-processed data. Note that we counted only motile bacteria, to account for the wall accumulation effect, excluding sedimented cells of which displacements over 1.8 sec were less than one body length (~ 10 μ m). We found that over 85% of the total population were motile.

D. Model calculation

We performed numerical calculations for our theoretical model using Mathematica 14.3 (Wolfram). The steady-state distributions of bacteria and oxygen were obtained by solving Equations (1) and (5) satisfying $\int_0^h B(y) dy = B_{\text{tot}}$. The equations were nondimensionalized as shown in the Supplementary Materials and solved numerically with the following boundary conditions. For bacteria, no-flux boundary conditions are imposed at both surfaces ($y = 0, h$). For oxygen, the bottom surface ($y = 0$) is also a no-flux boundary, while the oxygen can be supplied from the top surface ($y = h$). Avoiding numerical instability, we implement a Dirichlet boundary condition at the top, $c(y = h) = c_h$, and determine the value of c_h self-consistently. Namely, at the steady-state with c_h , the total oxygen flux entering through the top boundary, $J_{\text{oxy}}(c_h)$, equals the total consumption rate by all bacteria in the film, $R_{\text{tot}}(c_h)$. Specifically, at the steady state, the oxygen flux was given by $J_{\text{oxy}} = -D_{\text{cover}} \frac{c_{\text{air}} - c_h}{h_{\text{cover}}}$, where D_{cover} was the oxygen diffusion coefficient in the oxygen-permeable coverslip, c_{air} is the oxygen concentration in ambient air, and h_{cover} is the thickness of the coverslip. We adopted $D_{\text{cover}} = 3.19 \times 10^{-1}$ $\mu\text{m}^2/\text{s}$ and $h_{\text{cover}} = 180$ μm and searched c_h that satisfied the steady-state condition with the range of $5 \times 10^{-5} c_0$ and c_0 , where c_0 denotes the saturated oxygen concentration in water. When the computed value exceeded c_0 , we set $c_h = c_0$. We found that all c_h values in our calculations were above the motility threshold, at which cells lose their motility at $c_h < 5 \times 10^{-5} c_0$ [42]. Lastly, we do not show extremely asymmetric solutions ($sym < 0.17$) in Fig. 4, as they often fail to satisfy the boundary conditions numerically.

- [1] T. Fenchel, Microbial behavior in a heterogeneous world, *Science* **296**, 1068 (2002).
- [2] M. R. Spratt and K. Lane, Navigating environmental transitions: The role of phenotypic variation in bacterial responses, *mBio* **13**, e02212 (2022).
- [3] J. M. Keegstra, F. Carrara, and R. Stocker, The ecological roles of bacterial chemotaxis, *Nature Reviews Microbiology* **20**, 491 (2022).
- [4] V. Piskovsky and N. M. Oliveira, Bacterial motility can govern the dynamics of antibiotic resistance evolution, *Nature Communications* **14**, 5584 (2023).
- [5] R. Porter, C. Trenado-Yuste, A. Martinez-Calvo, M. Su, N. S. Wingreen, S. S. Datta, and K. C. Huang, On the growth and form of bacterial colonies, *Nature Reviews Physics* **7**, 535 (2025).
- [6] C. Douarche, A. Buguin, H. Salman, and A. Libchaber, *E. coli* and oxygen: A motility transition, *Physical Review Letters* **102**, 198101 (2009).
- [7] J. Bouvard, C. Douarche, P. Mergaert, H. Auradou, and F. Moisy, Direct measurement of the aerotactic response in a bacterial suspension, *Physical Review E* **106**, 034404 (2022).
- [8] B. C. Mazzag, I. B. Zhulin, and A. Mogilner, Model of bacterial band formation in aerotaxis, *Biophysical Journal* **85**, 3558 (2003).
- [9] F. Menolascina, R. Rusconi, V. I. Fernandez, S. Smriga, Z. Aminzare, E. D. Sontag, and R. Stocker, Logarithmic sensing in *bacillus subtilis* aerotaxis, *npj Systems Biology and Applications* **3**, 16036 (2017).
- [10] A. P. Berke, L. Turner, H. C. Berg, and E. Lauga, Hydrodynamic attraction of swimming microorganisms by surfaces, *Physical Review Letters* **101**, 038102 (2008).
- [11] G. Li and J. X. Tang, Accumulation of microswimmers near a surface mediated by collision and rotational brownian motion, *Physical Review Letters* **103**, 078101 (2009).
- [12] P. Sartori, E. Chiarello, G. Jayaswal, M. Pierno, G. Mistura, P. Brun, A. Tiribocchi, and E. Orlandini, Wall accumulation of bacteria with different motility patterns, *Physical Review E* **97**, 022610 (2018).
- [13] C. Li, H. Bian, Y. Qiao, J. Zhu, and Z. Qu, Hydrodynamic interaction leads to the accumulation of *chlamydomonas reinhardtii* near a solid-liquid interface, *Physical Review E* **111**, L052401 (2025).
- [14] J. C. Conrad, Physics of bacterial near-surface motility using flagella and type iv pili: implications for biofilm formation, *Research in Microbiology* **163**, 619 (2012).
- [15] C. A. Fux, J. W. Costerton, P. S. Stewart, and P. Stoodley, Survival strategies of infectious biofilms, *Trends in Microbiology* **13**, 34 (2005).
- [16] H. H. Tuson and D. B. Weibel, Bacteria-surface interactions, *Soft Matter* **9**, 4368 (2013).
- [17] G. Jing, A. Zlotnik, C. Lindner, Chirality-induced bacterial rheotaxis in bulk shear flows, *Science Advances* **6**, eabb2012 (2020).
- [18] A. Ramamonjy, J. Dervaux, and P. Brunet, Nonlinear phototaxis and instabilities in suspensions of light-seeking algae, *Physical Review Letters* **128**, 258101 (2022).
- [19] A. Carrere, J. Lessandro, O. Cochet-Escartin, J. Hesnard, N. Ghazi, C. Riviere, C. Anjard, F. Detcheverry, and J.-P. Rieu, Microphase separation of living cells, *Nature Communications* **14**, 796 (2023).
- [20] P. Prakash, Y. Baig, F. J. Peaudecerf, and R. E. Goldstein, Dynamics of an algae-bacteria microcosm: Photosynthesis, chemotaxis, and expulsion in inhomogeneous active matter, *Proceedings of the National Academy of Sciences* **122**, e2410225122 (2025).
- [21] I. Eisenmann, M. Vona, N. Desprat, T. Ishikawa, E. Lauga, and R. Jeanneret, Pure hydrodynamic instabilities in active jets of puller microalgae, *Physical Review Letters* **135**, 198301 (2025).
- [22] Rothschild, Non-random Distribution of Bull Spermatozoa in a Drop of Sperm Suspension, *Nature* **198**, 1221 (1963).
- [23] I. Vladescu, E. Marsden, J. Schwarz-Linek, V. Martinez, J. Arlt, A. Morozov, D. Marenduzzo, M. Cates, and W. Poon, Filling an emulsion drop with motile bacteria, *Physical Review Letters* **113**, 268101 (2014).
- [24] H. Wioand, F. G. Woodhouse, J. Dunkel, J. O. Kessler, and R. E. Goldstein, Confinement Stabilizes a Bacterial Suspension into a Spiral Vortex, *Physical Review Letters* **110**, 268102 (2013).
- [25] D. Nishiguchi, I. S. Aranson, A. Snezhko, and A. Sokolov, Engineering bacterial vortex lattice via direct laser lithography, *Nature Communications* **9**, 4486 (2018).
- [26] H. Xu, J. Dauparas, D. Das, E. Lauga, and Y. Wu, Self-organization of swimmers drives long-range fluid transport in bacterial colonies, *Nature Communications* **10**, 1792 (2019).
- [27] S. E. Hulme, W. R. DiLuzio, S. S. Shevkoplyas, L. Turner, M. Mayer, H. C. Berg, and G. M. Whitesides, Using ratchets and sorters to fractionate motile cells of *escherichia coli* by length, *Lab on a Chip* **8**, 1888 (2008).
- [28] G. Lambert, D. Liao, and R. H. Austin, Collective escape of chemotactic swimmers through microscopic ratchets, *Physical Review Letters* **104**, 168102 (2010).
- [29] P. Denissenko, V. Kantsler, D. J. Smith, and J. Kirkman-Brown, Human spermatozoa migration in microchannels reveals boundary-following navigation, *Proceedings of the National Academy of Sciences* **109**, 8007 (2012).
- [30] S. Coppola and V. Kantsler, Curved ratchets improve bacteria rectification in microfluidic devices, *Physical Review E* **104**, 014602 (2021).
- [31] S. Anand, X. Ma, S. Guo, S. Martiniani, and X. Cheng, Transport and energetics of bacterial rectification, *Proceedings of the National Academy of Sciences* **121**, e2411608121 (2024).
- [32] M. Adler, M. Erickstad, E. Gutierrez, and A. Groisman, Studies of bacterial aerotaxis in a microfluidic device, *Lab on a Chip* **12**, 4835 (2012).
- [33] N. M. Oliveira, K. R. Foster, and W. M. Durham, Single-cell twitching chemotaxis in developing biofilms, *Proceedings of the National Academy of Sciences* **113**, 6532 (2016).
- [34] M. M. Salek, F. Carrara, V. Fernandez, J. S. Guasto, and R. Stocker, Bacterial chemotaxis in a microfluidic t-maze reveals strong phenotypic heterogeneity in chemotactic sensitivity, *Nature Communications* **10**, 10.1038/s41467-019-09521-2 (2019).
- [35] J. Adler, Chemotaxis in bacteria: Motile *escherichia coli* migrate in bands that are influenced by oxygen and or-

- ganic nutrients., *Science* **153**, 708-716 (1966).
- [36] I. B. Zhulin, V. A. Bespalov, M. S. Johnson, and B. L. Taylor, Oxygen taxis and proton motive force in *azospirillum brasilense*, *Journal of Bacteriology* **178**, 5199 (1996).
- [37] T. V. Phan, H. H. Mattingly, L. Vo, J. S. Marvin, L. L. Looger, and T. Emonet, Direct measurement of dynamic attractant gradients reveals breakdown of the patlak? Keller-Segel chemotaxis model, *Proceedings of the National Academy of Sciences* **121**, e2309251121 (2024).
- [38] C. Jin and A. Sengupta, Microbes in porous environments: from active interactions to emergent feedback, *Biophysical Reviews* **16**, 173 (2024).
- [39] T. Bhattacharjee, D. B. Amchin, J. A. Ott, F. Kratz, and S. S. Datta, Chemotactic migration of bacteria in porous media, *Biophysical Journal* **120**, 3483 (2021).
- [40] K. Aleklett, E. T. Kiers, P. Ohlsson, T. S. Shimizu, V. E. A. Caldas, and E. C. Hammer, Build your own soil: exploring microfluidics to create microbial habitat structures, *The ISME Journal* **12**, 312 (2018).
- [41] S. E. Spagnolie and E. Lauga, Hydrodynamics of self-propulsion near a boundary: predictions and accuracy of far-field approximations, *Journal of Fluid Mechanics* **700**, 105 (2012).
- [42] B. V. Hokmabad, A. Martínez-Calvo, S. Gonzalez La Corte, and S. S. Datta, Spatial self-organization of confined bacterial suspensions, *Proceedings of the National Academy of Sciences* **122**, e2503983122 (2025).
- [43] E. F. Keller and L. A. Segel, Model for chemotaxis, *Journal of Theoretical Biology* **30**, 225 (1971).
- [44] E. F. Keller and L. A. Segel, Traveling bands of chemotactic bacteria: A theoretical analysis, *Journal of Theoretical Biology* **30**, 235 (1971).
- [45] W. Zhang, J. S. Olson, and G. N. Phillips Jr., Biophysical and kinetic characterization of hemat, an aerotaxis receptor from *Bacillus subtilis*, *Biophysical Journal* **88**, 2801 (2005).
- [46] J. Ainley, S. Durkin, R. Embid, P. Boindala, and R. Cortez, The method of images for regularized stokeslets, *Journal of Computational Physics* **227**, 4600 (2008).
- [47] L. H. Cisneros, J. O. Kessler, R. Ortiz, R. Cortez, and M. A. Bees, Unexpected bipolar flagellar arrangements and long-range flows driven by bacteria near solid boundaries, *Physical Review Letters* **101**, 168102 (2008).
- [48] B. Zhao, E. Lauga, and L. Koens, Method of regularized stokeslets: Flow analysis and improvement of convergence, *Physical Review Fluids* **4**, 084104 (2019).
- [49] I. Tuval, L. Cisneros, C. Dombrowski, C. W. Wolgemuth, J. O. Kessler, and R. E. Goldstein, Bacterial swimming and oxygen transport near contact lines, *Proceedings of the National Academy of Sciences of the United States of America* **102**, 2277 (2005).
- [50] J. Cheon, J. Son, S. Lim, Y. Jeong, J.-H. Park, R. J. Mitchell, J. U. Kim, and J. Jeong, Motile bacteria crossing liquid-liquid interfaces of an aqueous isotropic-nematic coexistence phase, *Soft Matter* **20**, 7313 (2024).
- [51] J. Najafi, F. Altegoer, G. Bange, and C. Wagner, Swimming of bacterium *Bacillus subtilis* with multiple bundles of flagella, *Soft Matter* **15**, 10029 (2019).
- [52] R. Nock and F. Nielsen, Statistical region merging, *IEEE Transactions on Pattern Analysis and Machine Intelligence* **26**, 1452 (2004).

Density-Dependent Transition in Bacterial Self-Organization Driven by Confinement and Aerotaxis

Minjun Kim¹ and Joonwoo Jeong^{1,2,*}

¹*Department of Physics, Ulsan National Institute of Science and Technology, Ulsan, Republic of Korea*

²*UNIST Center for Soft and Living Matter, Ulsan, Korea*

(Dated: March 17, 2026)

I. CONTROL EXPERIMENTS VERIFYING AEROTACTIC MIGRATION

To confirm that the aerotaxis drove the asymmetric distribution at high number density, we conducted control experiments (Sup. Fig. S1). First, in (a), inverting the entire liquid film, caused the bacterial accumulation to shift toward the newly oxygen-supplied boundary. Second, in (b), replacing the impermeable spacer with a gas-permeable one, which creates both vertical and radial oxygen gradients, eliminated the asymmetric profile. Finally, in (c), to exclude any substrate-preference effects, we placed the air-permeable coverslip on the bottom the glass substrate. To maintain the same oxygen pathway, epoxy was spread over the bottom surface to prevent additional oxygen supply from the bottom. This substrate was degassed in a vacuum chamber for one hour to remove trapped oxygen, followed by nitrogen replacement overnight. We observed that the overall distribution remained asymmetric.

To further validate, we performed experiments using a gas-controlled chamber (Sup. Fig. S2). An intermediate number density sample ($B_{\text{tot}} = 6.3 \times 10^7$ cells/mL) was exposed to an external oxygen concentration of 5%. As a result, an asymmetric distribution was observed under hypoxia (5%) even at a lower cell density compared to the ambient-air experiment (21%, $B_{\text{tot}} = 7.6 \times 10^7$ cells/mL), confirming that the migration is oxygen-driven.

II. INDEPENDENCE OF VERTICAL DISTRIBUTION FROM SPATIAL INHOMOGENEITY

We identified the total number density (B_{tot}) as the key parameter determining the dominant mechanism in our confined liquid film system. However, local density fluctuations could potentially modify the oxygen concentration, leading to spatially varying distributions across the film. Such population heterogeneity had been reported in free-standing liquid films thicker than 200 μm [1, 2]. To investigate this, we intentionally induced spatial inhomogeneity in a confined film by sealing a narrow sandwich-like gap filled with bacterial suspension using curing epoxy. The uncured epoxy acted as a chemo-repellent, causing the bacterial density to peak at the center in low B_{tot} suspensions (Sup. Fig. S3(a), (b)). Notably, in the low B_{tot} case, the local number density at the center exceeded the density of the intermediate B_{tot} case. We measured bacterial distributions at three positions: the center and two midway points between the epoxy edge and the center. Similar to Sup. Fig. S1, the symmetry of the bacterial profile depended on B_{tot} , indicating that global bacterial respiration and oxygen concentration play important roles in determining the spatial distribution.

III. REGULARIZED STOKESLET

To avoid divergence at the top and bottom boundaries, we employed the regularized Stokeslet for $u_{\text{hydro}} = -k(\frac{1}{y^2} - \frac{1}{(h-y)^2})$ [3]. Starting from the expression of a normal Stokeslet for a dipole, the flow velocity was calculated as follow:

$$u^{\text{dipole}}(\mathbf{r}) = \frac{1}{4\pi\eta} \left(\frac{\mathbf{q}}{r^3} - \frac{3(\mathbf{q} \cdot \mathbf{r})\mathbf{r}}{r^5} \right) \quad (\text{S1})$$

where \mathbf{q} is the dipole moment [4]. By selected the most general blob function $\phi_\epsilon(r) = \frac{15\epsilon^4}{8\pi(r^2 + \epsilon^2)^{7/2}}$, the regularized Stokeslet became,

$$u_\epsilon^{\text{dipole}}(\mathbf{r}) = \frac{1}{4\pi\eta} \left(\frac{\mathbf{q}}{(r^2 + \epsilon^2)^{3/2}} - \frac{3(\mathbf{q} \cdot \mathbf{r})\mathbf{r}}{(r^2 + \epsilon^2)^{5/2}} \right) - \frac{3\epsilon^2\mathbf{q}}{(r^2 + \epsilon^2)^{5/2}} \approx \frac{1}{4\pi\eta} \left(\frac{\mathbf{q}}{(r^2 + \epsilon^2)^{3/2}} - \frac{3(\mathbf{q} \cdot \mathbf{r})\mathbf{r}}{(r^2 + \epsilon^2)^{5/2}} \right). \quad (\text{S2})$$

* jjeong@unist.ac.kr

Comparing equations (1) and (2), we noticed that r was replaced by $\sqrt{r^2 + \epsilon^2}$. Consequently, the hydrodynamic advection was modified to:

$$u_{\text{hydro}} = -k \left(\frac{1}{y^2 + \epsilon^2} - \frac{1}{(h-y)^2 + \epsilon^2} \right) \quad (\text{S3})$$

IV. NONDIMENSIONALIZED MODEL

We nondimensionalized equations (1) and (5) from the main text and solved them numerically. First, the equation for oxygen concentration was modified as follows:

$$\begin{aligned} \frac{c_0 \partial \theta(\eta, \tau)}{\tau_0 \partial \tau} &= \frac{D_{\text{oxy}} c_0}{h^2} \frac{\partial^2 \theta(\eta, \tau)}{\partial \eta^2} - \frac{B_{\text{tot}} R_0}{2} \left(\frac{\theta(\eta, \tau)}{\theta(\eta, \tau) + K_{\text{d1}}/c_0} + \frac{\theta(\eta, \tau)}{\theta(\eta, \tau) + K_{\text{d2}}/c_0} \right) \xi(\eta, \tau) \\ \frac{\partial \theta(\eta, \tau)}{\partial \tau} &= \frac{D_{\text{oxy}} \tau_0}{h^2} \frac{\partial^2 \theta(\eta, \tau)}{\partial \eta^2} - \frac{\tau_0 B_{\text{tot}} R_0}{2c_0} \left(\frac{\theta(\eta, \tau)}{\theta(\eta, \tau) + K'_{\text{d1}}} + \frac{\theta(\eta, \tau)}{\theta(\eta, \tau) + K'_{\text{d2}}} \right) \xi(\eta, \tau) \end{aligned} \quad (\text{S4})$$

where η and τ are the nondimensionalized position and time, respectively. Here, $\theta(\eta, \tau) = c(y, t)/c_0$ and $\xi(\eta, \tau) = B(y, t)/B_{\text{tot}}$ represent the nondimensionalized oxygen concentration and bacterial density. c_0 is the oxygen saturation concentration in water at room temperature, and B_{tot} is the total bacteria number density. $K'_{\text{d1}} = K_{\text{d1}}/c_0$ and $K'_{\text{d2}} = K_{\text{d2}}/c_0$ are the nondimensionalized oxygen dissociation constants. We defined $\tau_0 = h^2/D_{\text{oxy}}$ as the characteristic diffusion time of oxygen. Equation (4) was rewritten as:

$$\begin{aligned} \frac{\partial \theta(\eta, \tau)}{\partial \tau} &= \frac{\partial^2 \theta(\eta, \tau)}{\partial \eta^2} - \frac{B_{\text{tot}} h^2 R_0}{2c_0 D_{\text{oxy}}} \left(\frac{\theta(\eta, \tau)}{\theta(\eta, \tau) + K'_{\text{d1}}} + \frac{\theta(\eta, \tau)}{\theta(\eta, \tau) + K'_{\text{d2}}} \right) \xi(\eta, \tau) \\ \frac{\partial \theta(\eta, \tau)}{\partial \tau} &= \frac{\partial^2 \theta(\eta, \tau)}{\partial \eta^2} - R' \xi(\eta, \tau) \end{aligned} \quad (\text{S5})$$

where $R' = \frac{R_0}{2} \left(\frac{\theta(\eta, \tau)}{\theta(\eta, \tau) + K'_{\text{d1}}} + \frac{\theta(\eta, \tau)}{\theta(\eta, \tau) + K'_{\text{d2}}} \right)$ and $R'_0 = \frac{B_{\text{tot}} h^2 R_0}{c_0 D_{\text{oxy}}}$.

Next, the equation for bacterial distribution was modified as follows:

$$\begin{aligned} \frac{B_{\text{tot}} \partial \xi(\eta, \tau)}{\tau_0 \partial \tau} &= \frac{1}{h} \frac{\partial}{\partial \eta} \left[D_{\text{bac}} \frac{B_{\text{tot}} \partial \xi(\eta, \tau)}{h \partial \eta} - u(y, t) B_{\text{tot}} \xi(\eta, \tau) \right], \\ \frac{\partial \xi(\eta, \tau)}{\partial \tau} &= \frac{\partial}{\partial \eta} \left[d \frac{\partial \xi(\eta, \tau)}{\partial \eta} - \frac{h}{D_{\text{oxy}}} (u_{\text{hydro}}(y, t) + u_{\text{taxis}}(y, t)) \xi(\eta, \tau) \right] \end{aligned} \quad (\text{S6})$$

where $d = D_{\text{bac}}/D_{\text{oxy}}$. The advection velocities were transformed as:

$$\begin{aligned} u_{\text{hydro}}(y, t) &= -k \left(\frac{1}{y^2} - \frac{1}{(h-y)^2} \right) = -\frac{k}{h^2} \left(\frac{1}{\eta^2} - \frac{1}{(1-\eta)^2} \right), \\ u_{\text{taxis}}(y, t) &= \chi \frac{\partial c(y, t)/\partial y}{(c(y, t) + K_{\text{d1}})(c(y, t) + K_{\text{d2}})} = \frac{\chi}{hc_0} \frac{\partial \theta(\eta, \tau)/\partial \eta}{(\theta(\eta, \tau) + K'_{\text{d1}})(\theta(\eta, \tau) + K'_{\text{d2}})} \end{aligned}$$

Combining these, the final equation became:

$$\begin{aligned} \frac{\partial \xi(\eta, \tau)}{\partial \tau} &= \frac{\partial}{\partial \eta} \left[d \frac{\partial \xi(\eta, \tau)}{\partial \eta} + \left(\frac{k}{D_{\text{oxy}} h} \left(\frac{1}{\eta^2} - \frac{1}{(1-\eta)^2} \right) - \frac{\chi}{D_{\text{oxy}} c_0} \frac{\partial \theta(\eta, \tau)/\partial \eta}{(\theta(\eta, \tau) + K'_{\text{d1}})(\theta(\eta, \tau) + K'_{\text{d2}})} \right) \xi(\eta, \tau) \right], \\ \frac{\partial \xi(\eta, \tau)}{\partial \tau} &= \frac{\partial}{\partial \eta} \left[d \frac{\partial \xi(\eta, \tau)}{\partial \eta} + \left(k' \left(\frac{1}{\eta^2} - \frac{1}{(1-\eta)^2} \right) - \chi' \frac{\partial \theta(\eta, \tau)/\partial \eta}{(\theta(\eta, \tau) + K'_{\text{d1}})(\theta(\eta, \tau) + K'_{\text{d2}})} \right) \xi(\eta, \tau) \right] \end{aligned} \quad (\text{S7})$$

where $k' = k/D_{\text{oxy}}h$ and $\chi' = \chi/D_{\text{oxy}}c_0$ represent the nondimensionalized hydrodynamic strength and aerotactic sensitivity, respectively.

The boundary conditions were set as follows: for equation (5) (oxygen),

$$\left. \frac{\partial \theta(\eta, \tau)}{\partial \eta} \right|_{\eta=0} = 0$$

$$\theta(\eta = 1, \tau) = c_h/c_0 = c'_h$$

For equation (7) (bacteria),

$$\left[d \frac{\partial \xi(\eta, \tau)}{\partial \eta} + \left(k' \left(\frac{1}{\eta^2} - \frac{1}{(1-\eta)^2} \right) - \chi' \frac{\partial \theta(\eta, \tau)/\partial \eta}{(\theta(\eta, \tau) + K'_{d1})(\theta(\eta, \tau) + K'_{d2})} \right) \xi(\eta, \tau) \right] \Big|_{\eta=0} = 0$$

$$\int_0^1 \xi(\eta) d\eta = 1.0$$

As explained in the main text, the boundary condition $\theta(\eta = 1, \tau) = c'_h$ was determined by balancing the nondimensionalized total respiration rate and oxygen flux.

V. EXTENDED MODEL CALCULATION

The model calculations for extended ranges of B_{tot} and h are shown in Fig. S5. Below, we discuss two extreme regimes in the phase diagram where additional physical effects become relevant.

For sub-millimeter film heights (h) and high total bacterial densities (B_{tot}), we must consider bioconvection—a phenomenon arising from the competition between aerotactic migration and gravitational instability [5–7]. Specifically, the highly asymmetric bacterial distribution creates a density inversion, triggering Rayleigh-Taylor instability. This causes bacterial plumes to descend toward the bottom, while the vertical oxygen gradient drives them to migrate upward again. This interplay generates macroscopic convection rolls, manifesting as various bioconvective patterns depending on film height and bacterial species [6, 7]. However, in our experiments, we did not observe such bioconvective patterns, even under conditions yielding strongly asymmetric profiles. To assess the stability of our system, we calculate the Rayleigh number ($Ra = \Delta \rho g h^3 / D_{\text{bac}} \mu$), a dimensionless parameter characterizing the onset of bioconvection. Previous experimental studies reporting robust bioconvection typically involved Rayleigh numbers in the thousands, although numerical simulations suggest a critical value of $Ra_{\text{crit}} \approx 500$ [5]. In our experimental setup, the maximum estimated Rayleigh number is $Ra = 4.64$. This value is well below the critical threshold, confirming that the system remains stable without forming bioconvective instabilities. Our model predicts that the system would transition into the bioconvection regime at larger h and B_{tot} , yielding Ra values exceeding Ra_{crit} ; however, this regime lies beyond the scope of the current study.

A recent paper reports that wall accumulation weakens and bulk concentration increases as film height decreases [8]. This phenomenon is attributed to the hydrodynamic quadrupole flow, which exerts a torque that reorients bacteria toward the middle of film, consequently reducing boundary accumulation. This bulk-concentrating effect becomes significant for heights $h \leq 30 \mu\text{m}$, a range covered by our calculations in Fig. S5. Our model, based on regularized dipole hydrodynamic interactions, predicts a persistent strong wall accumulation ($B(h/2)/B_{\text{max}} < 0.25$) even in this regime. Notably, our model bacteria, *B. subtilis* exhibits a significantly lower central density ($B(h/2)/B_{\text{max}} \sim 0.1$) at $h \sim 80 \mu\text{m}$ compared to *E. coli* (~ 0.4). This suggests that a model excluding quadrupole terms provides a better prediction for *B. subtilis* at these typical heights. Such species-specific differences make a direct comparison difficult and warrant further investigation into factors such as propulsive force and flagellar bundling dynamics [3, 9–12].

-
- [1] A. Sokolov, R. E. Goldstein, F. I. Feldchtein, and I. S. Aranson, Enhanced mixing and spatial instability in concentrated bacterial suspensions, *Physical Review E* **80**, 031903 (2009).
 - [2] B. Ezhilan, A. A. Pahlavan, and D. Saintillan, Chaotic dynamics and oxygen transport in thin films of aerotactic bacteria, *Physics of Fluids* **24**, 091701 (2012).
 - [3] A. P. Berke, L. Turner, H. C. Berg, and E. Lauga, Hydrodynamic attraction of swimming microorganisms by surfaces, *Physical Review Letters* **101**, 038102 (2008).

- [4] J. Ainley, S. Durkin, R. Embid, P. Boindala, and R. Cortez, The method of images for regularized stokeslets, *Journal of Computational Physics* **227**, 4600 (2008).
- [5] H. Yanaoka and T. Nishimura, Pattern wavelengths and transport characteristics in three-dimensional bioconvection generated by chemotactic bacteria, *Journal of Fluid Mechanics* **952**, A13 (2022).
- [6] O. Gallardo-Navarro, R. Arbel-Goren, E. August, G. Olmedo-Alvarez, and J. Stavans, Dynamically induced spatial segregation in multispecies bacterial bioconvection, *Nature Communications* **16**, 950 (2025).
- [7] D. Shoup and T. Ursell, Bacterial bioconvection confers context-dependent growth benefits and is robust under varying metabolic and genetic conditions, *Journal of Bacteriology* **205**, e00232 (2023).
- [8] D. Wei, S. Hu, T. Tang, Y. Yang, F. Meng, and Y. Peng, Confinement reduces surface accumulation of swimming bacteria, *Physical Review Letters* **135**, 188401 (2025).
- [9] J. Cheon, J. Son, S. Lim, Y. Jeong, J.-H. Park, R. J. Mitchell, J. U. Kim, and J. Jeong, Motile bacteria crossing liquid–liquid interfaces of an aqueous isotropic–nematic coexistence phase, *Soft Matter* **20**, 7313 (2024).
- [10] J. Najafi, F. Altegoer, G. Bange, and C. Wagner, Swimming of bacterium *Bacillus subtilis* with multiple bundles of flagella, *Soft Matter* **15**, 10029 (2019).
- [11] G. Junot, T. Darnige, A. Lindner, V. A. Martinez, J. Arlt, A. Dawson, W. C. K. Poon, H. Auradou, and E. Clément, Run-to-tumble variability controls the surface residence times of *E. coli* bacteria, *Physical Review Letters* **128**, 248101 (2022).
- [12] A. G. Prabhune, A. S. García-Gordillo, I. S. Aranson, T. R. Powers, and N. Figueroa-Morales, Bacteria navigate anisotropic media using a flagellar tug-of-oars, *PRX Life* **2**, 033004 (2024).

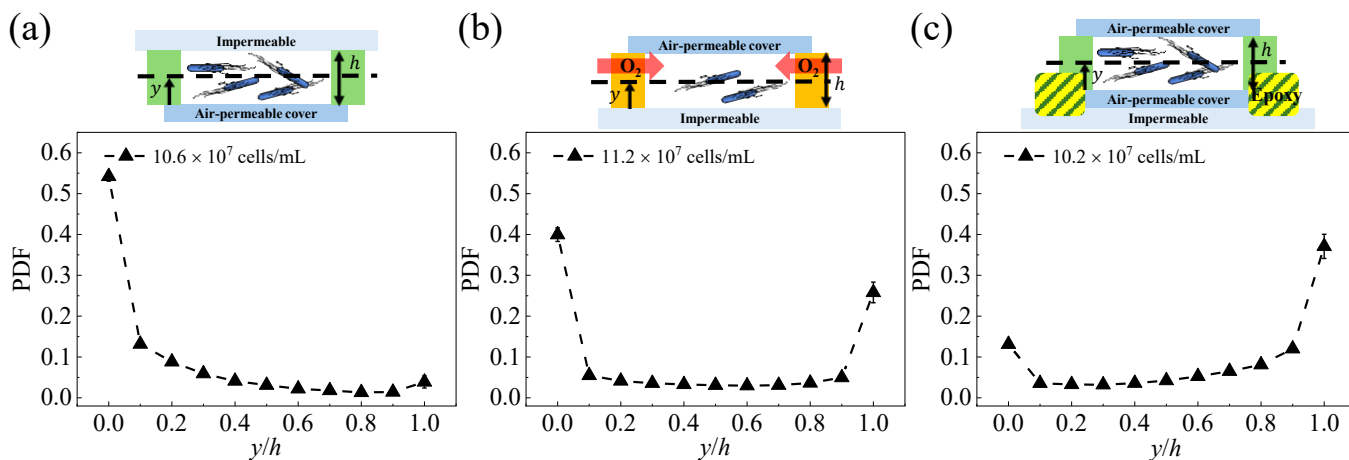


FIG. S1. Control experiments to test the aerotaxis hypothesis. A series of experiments was conducted to verify whether aerotaxis was the primary reason for the asymmetric bacterial profile. (a) The liquid film was inverted (flipped). Despite the inversion, the bacterial peak remained at the oxygen-supplied boundary ($y/h = 1$). (b) The spacer was replaced with an air-permeable material (PDMS) to induce an oxygen gradient in the radial direction of the well. This setup resulted in a symmetric bacterial distribution, even under high B_{tot} . (c) A potential substrate-preference effect was investigated. An air-permeable substrate was attached to the bottom, the liquid film was assembled, and epoxy was spread over the bottom to prevent additional oxygen supply. An asymmetric distribution was still observed. Residual oxygen trapped during film assembly, rather than a substrate preference, might be the cause of the bacteria remaining at the bottom.

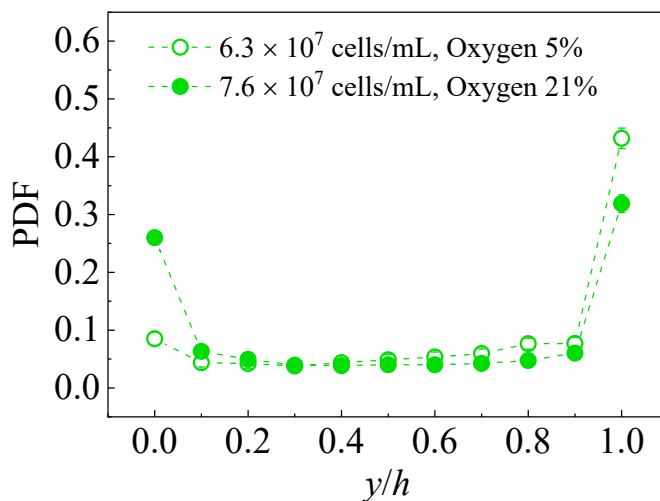


FIG. S2. Probability density function (PDF) of bacterial distributions under controlled external oxygen concentration. The experiment compares a hypoxia condition (5% O_2 , 6.3×10^7 cells/mL; open circles) with an ambient-air condition (21% O_2 , 7.6×10^7 cells/mL; filled circles). For this experiment, a liquid film was placed in a gas-mixing chamber, and gases with specific oxygen concentrations were injected. The x-axis represents the normalized vertical position (y/h), and error bars indicate temporal fluctuation, as in Fig. S1. Notable, an asymmetric distribution was observed under hypoxia (5%), even at a lower cell density compared to the ambient-air experiment (21%).

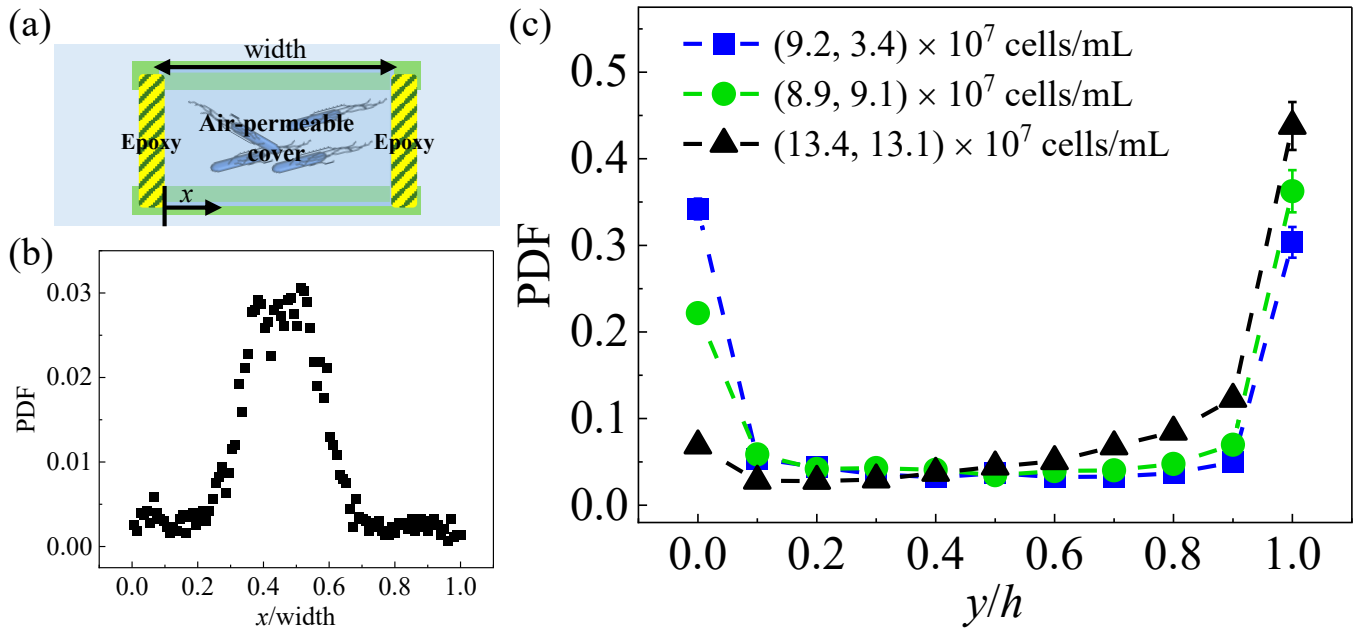


FIG. S3. Setup for the spatial heterogeneity experiment and resulting bacterial distribution at different local number densities. (a) Schematic of the experimental setup. An impermeable spacer was used to define the channel geometry, and the bacterial suspension was filled into the narrow gap by capillary flow. The entrance and exit were subsequently sealed with epoxy to prevent evaporation and induce negative chemotaxis. The direction from the entrance is defined as x and the width represents the distance between the two epoxy boundaries. (b) Spatial inhomogeneity was observed in the low cell density suspension. The bacterial population was measured along the horizontal (x) direction, and the PDF was plotted as a function of the normalized position (x/width). The bacterial density exhibited a peak at the center. (c) Steady-state distributions of bacteria measured at the central region for different total densities: blue squares (low), green circles (intermediate), and black triangles (high). The legend values denote $(B_{\text{local}}, B_{\text{tot}})$ representing the local number density at the center and the total density for each suspension, respectively.

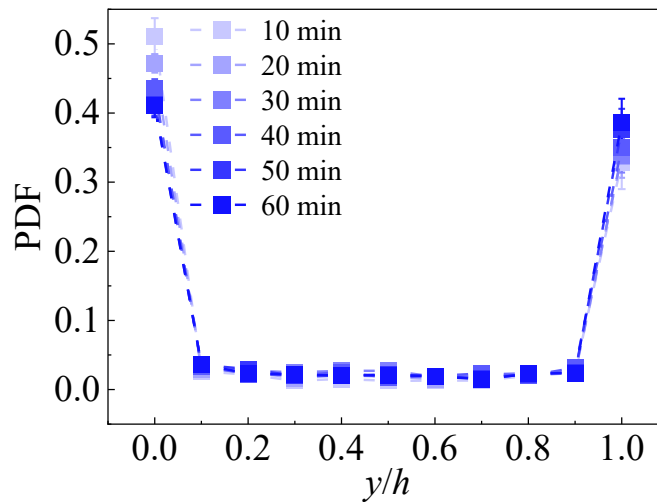


FIG. S4. Temporal evolution of the bacterial distribution at low density. PDFs of bacterial distributions for a low-density suspension (3.8×10^7 cells/mL) measured at 10 min intervals. The distribution remains symmetric and stable throughout the observed period, unlike the high-density case.

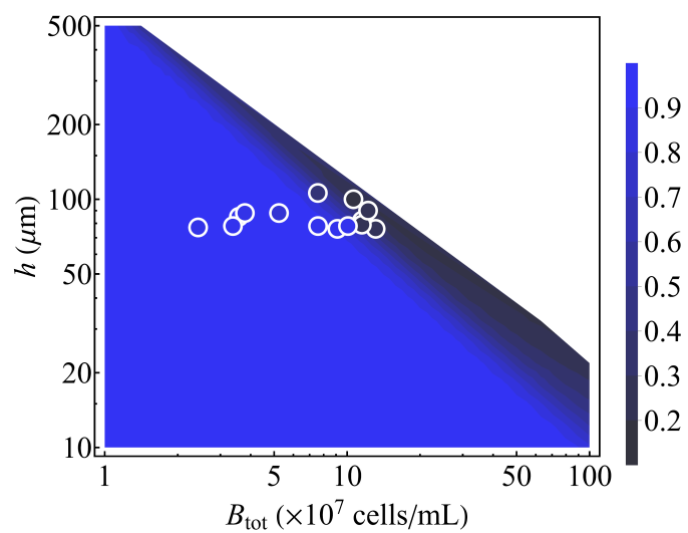


FIG. S5. The phase diagram of bacterial distribution symmetry over a broader range of B_{tot} and h . All other details, including the color scale and representation of experimental data, follow the same convention as in the main-text phase diagram.